JOURNAL OF THE AMERICAN HELICOPTER SOCIETY **67**, 022002 (2022)

# Nonlinear Aeroelastic Analysis for Highly Flexible Flapping Wing in Hover

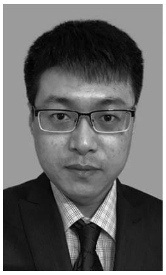


Xuan Yang*
*Research Assistant*

Aswathi Sudhir
*Research Assistant*

Atanu Halder
*Research Assistant*

Moble Benedict
*Associate Professor*

*Texas A & M University, College Station, TX*

**Aeromechanics of highly flexible flapping wings is a complex nonlinear fluid–structure interaction problem and, therefore, cannot be analyzed using conventional linear aeroelasticity methods. This paper presents a standalone coupled aeroelastic framework for highly flexible flapping wings in hover for micro air vehicle (MAV) applications. The MAV-scale flapping wing structure is modeled using fully nonlinear beam and shell finite elements. A potential-flow-based unsteady aerodynamic model is then coupled with the structural model to generate the coupled aeroelastic framework. Both the structural and aerodynamic models are validated independently before coupling. Instantaneous lift force and wing deflection predictions from the coupled aeroelastic simulations are compared with the force and deflection measurements (using digital image correlation) obtained from in-house flapping wing experiments at both moderate (13 Hz) and high (20 Hz) flapping frequencies. Coupled trim analysis is then performed by simultaneously solving wing response equations and vehicle trim equations until trim controls, wing elastic response, inflow and circulation converge all together. The dependence of control inputs on weight and center of gravity (cg) location of the vehicle is studied for the hovering flight case.**

## Nomenclature

| | |
|---|---|
| $B$ | Jaumann strain tensor |
| $D$ | displacement vector |
| $e_1$ | strains in $\eta$ directions |
| $e_2$ | strains in $\zeta$ directions |
| $F_i$ | residuals of trim functions |
| $J$ | Jaumann stress tensor |
| $K$ | stiffness matrix |
| $K_{(j)}$ | element stiffness matrix |
| $K_t$ | tangent stiffness matrix |
| $K_1$ | curvature matrix |
| $K_1^0$ | initial curvature matrix |
| $k_i$ | initial curvature |
| $M$ | mass matrix |
| $N$ | shape function matrix |
| $N_1$ | one-dimensional shape function matrix |
| $N_2$ | two-dimensional shape function matrix |
| $q$ | element displacement vector |
| $r$ | distance of center of thrust to center of vehicle |
| $T$ | transformation matrix |
| $T_L$ | thrust of left wing |
| $T_R$ | thrust of right wing |
| $U$ | local displacement vector |
| $V_{abc}$ | base vectors in frame abc |
| $V_\infty$ | free-stream flow velocity |
| $v_i$ | induced velocity at rotor–disk plane |
| $v_w$ | wake velocity |
| $W$ | weight of the vehicle |
| $W_{nc}$ | nonconservative external work |
| $w$ | out-of-plane deformation |
| $x_{cg}$ | center of gravity offset in the $x$ direction |
| $y_{cg}$ | center of gravity offset in the $y$ direction |
| $\beta$ | flap angle |
| $\Gamma$ | circulation |
| $\gamma$ | vorticity distribution |
| $\gamma_5$ | out-plane shear rotation angle |
| $\gamma_6$ | in-plane shear rotation angle |
| $\boldsymbol{\epsilon}$ | strain tensor |
| $\eta$ | airfoil camberline function |
| $\theta$ | wing pitch angle |
| $\theta_i$ | control parameters |
| $\Pi$ | potential energy |
| $\rho_i$ | deformed curvature |
| $\boldsymbol{\sigma}$ | stress tensor |
| $\Phi_w$ | Wagner function |
| $\phi_L$ | left wing midstroke angle |
| $\phi_R$ | right wing midstroke angle |
| $\varphi$ | strain vector |
| $\Psi_k$ | Kussner function |

*Corresponding author; email: xuan2017@tamu.edu.

Part of the paper was presented at AHS 73rd Annual Forum, Fort Worth, TX, May 9–11, 2017. Best Paper Award Winner in Modeling and Simulation Session.
Manuscript received December 2017; accepted October 2021.

DOI: 10.4050/JAHS.67.022002

## Introduction

Micro air vehicles (MAVs) have recently gained mainstream acceptance as a sophisticated and versatile variant of unmanned aerial vehicles. From being part of military strategies for performing nonintrusive surveillance in urban and constrained environments, to conducting search and rescue services, MAVs are changing human life in many aspects. Naturally, the curiosity of the scientific world has been roused further and, recently, more researchers have delved into the rigorous study of bioinspired flapping wing MAVs. Flapping wing MAVs, with their highly unsteady aerodynamic environment, are complex flight systems. They produce large instantaneous forces by generating high lift coefficients (Refs. 1, 2) and also provide higher control authority and robustness required to withstand disturbances such as wind gusts (Ref. 3). Over the past two decades, remarkable theoretical and experimental developments have been carried out in this field.

Conventional models for studying flapping wing aerodynamics generally rely on a rigid wing with prescribed flapping and pitching kinematics. However, a realistic flapping wing motivated by insects and hummingbirds is a highly intricate, anisotropic, flexible structure that undergoes large deflections during a flap cycle (Refs. 4, 5). Due to large inertial and aerodynamic forces acted on the wing, a flexible wing will undergo large dynamic shape changes including spanwise dynamic twist (even more than 60 deg from root to tip), large camber variations, contraction and expansion of wing surface, and transverse out-of-plane bending. Therefore, the effects of these shape changes on the lift and drag forces need to be accounted for in the aerodynamic model.

With certain wing shape and stiffness distribution, flexible flapping wings can produce significantly higher lift compared to rigid ones (Ref. 6). However, because of the small scale, high structural flexibility, nonuniformity in the distribution of mass and stiffness properties, highly nonlinear and unsteady aerodynamics, and the tight coupling between aerodynamics and structural dynamics, the analysis of a realistic flexible flapping wing is extremely challenging.

Most of the flapping wing aeroelastic models so far have been either high-fidelity computational fluid dynamics–computational structural dynamics (CFD–CSD) coupled solvers (Refs. 7, 8) or vortex-method based models (Ref. 9), which are computationally expensive, or lower order models with linear structural models (Ref. 10), which cannot capture the nonlinearities in a realistic flapping wing, especially while operating at high frequencies. Finding the balance between accuracy and computational cost is crucial, and different approaches have been adopted by researchers. CFD studies when coupled with a structural dynamics model would make the analysis extremely expensive. It is impractical to use such an analysis for routine design calculations of a flapping-wing system. Zbikowski (Ref. 11) used indicial functions to estimate the unsteady forces on a flapping wing in hover by separately modeling five different phenomena or components that contribute to the total force acting on the wing. Singh and Chopra (Ref. 10) coupled this aerodynamic model with a linear structural model to perform the aeroelastic analysis of an insect wing model. This work proved that the flexible flapping wing exhibited significant aeroelastic effects even at moderate frequencies (12 Hz). The unsteady vortex lattice and vortex methods have also been employed on flapping wing MAVs (Ref. 12). Ansari et al. (Refs. 13, 14) developed a circulation-based vortex method, which considers vortices shedding from both leading and trailing edges. This model demonstrated good agreement with the experimental work performed by Birch (Ref. 15). Gogulapati et al. (Ref. 16) have further improved this model by considering viscosity effects and also coupled it with a structural model for aeroelastic modeling of flexible insect-like wing.

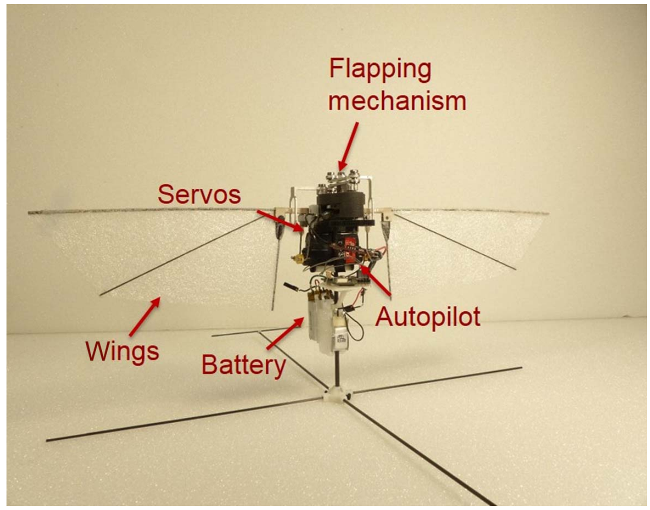


**Fig. 1. Flapping wing MAV developed in-house.**

Currently, as shown in Fig. 1, a hummingbird-inspired MAV has been developed and flight-tested in stable hover at Advanced Vertical Flight Laboratory at Texas A&M University (Ref. 17). This MAV has a gross weight of 62 g with 5-inch long wings flapping at about 20 Hz during hover. During the development of this vehicle, more than 50 different wing designs were tested to evaluate the performance before converging on the optimum design. This extensive and tedious method of designing the wing was the motivation for developing an accurate yet computationally efficient aeroelastic tool, which could be used for routine design calculations of such systems.

The in-house experimental studies conducted on this flapping wing demonstrated that at high frequencies (20 Hz) required for hovering, the wing undergoes large deflections (Ref. 18). Therefore, it is important to have a fully coupled nonlinear unsteady aeroelastic model to predict the performance of such a system. The eventual goal of this research is to incorporate this model as part of a flapping-wing MAV design framework that is currently being developed at Texas A&M University.

This paper describes the development of an aeroelastic model, which includes high-fidelity geometrically exact shell and beam-based wing structural model coupled with a potential flow-based unsteady indicial aerodynamic model that can also capture the effects of leading edge vortex, inflow, and shed wake. Furthermore, a coupled trim model is developed to predict the control inputs required for achieving force and moment equilibrium in hovering flight. Coupled trim analysis is performed by simultaneously solving wing response equations and vehicle trim equations until trim controls, wing elastic response, inflow, and circulation converge all together.

## Methodology

In the current analysis, an aeroelastic model of a flexible flapping wing is developed by coupling the potential-flow-based aerodynamic models with a geometrically exact nonlinear structural model, which reduces the computational cost yet perpetuates to provide reasonable results. The large deflections of the wing could be captured using the geometrically exact beam and plate-coupled model. The aerodynamic model adopted in this work is a potential-flow-based unsteady indicial model that could also capture the effects of leading edge vortex (using Polhamus leading edge suction analogy) and shed wake (through the Kussner function). An

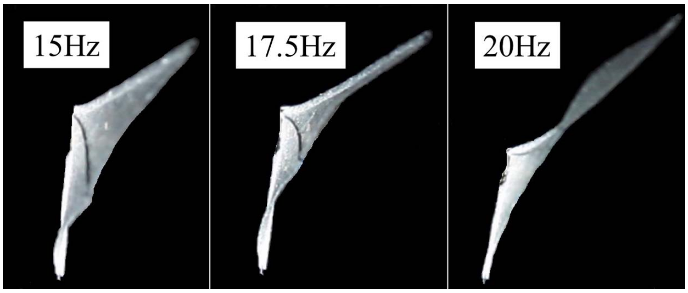


**Fig. 2. Wing deformation with varying frequency viewed edgewise down the wingspan (Ref. 17).**

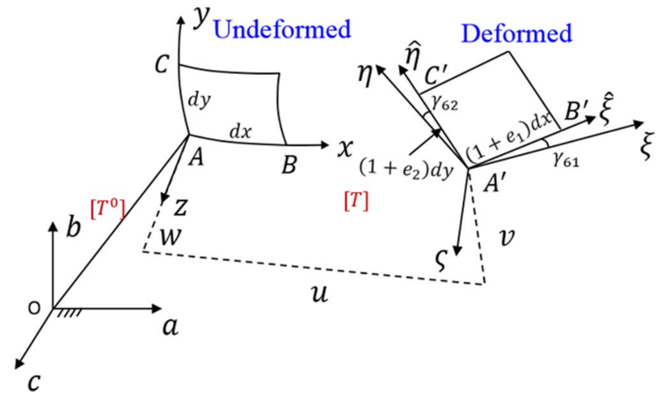


**Fig. 3. Undeformed and defor med geometries of differential reference surface with the corresponding coordinate systems (Ref. 21).**

innovative flapping wing test rig was designed and built to measure the time history of lift forces acting on a flexible wing during a flap cycle. The digital image correlation (DIC) technique is used to get deformed wing shape at different instants during a flap cycle and particle image velocimetry based flowfield measurements to analyze flow structures at different spanwise sections (Ref. 18).

Both aerodynamic and structural models are independently validated before coupling them to develop the aeroelastic framework. The aeroelastic simulation results are compared with test data; instantaneous lift force predictions with measured lift and wing deflections prediction are compared with the DIC measured deflections. The present aeroelastic framework, once validated, can serve as a platform to analyze different flapping-wing configurations in hovering state. The model will be later used in a design code to optimize the design of highly flexible flapping wings.

Coupled trim analysis requires simultaneous computation of trim controls, vehicle orientation, and wing elastic response so that both wing response equations and vehicle trim equations are satisfied. In this study, the dependence of control inputs on weight and longitudinal/lateral center of gravity (cg) offset of the vehicle is studied for hovering flight.

## Structural Model

The flapping wing structure analyzed in the current study is same as the one used on the in-house hover-capable robotic hummingbird shown in Fig. 1. The flapping wing utilizes passive wing deflections to achieve the optimum aerodynamic shape at the operational frequency. This requires the wing to be highly flexible and undergoes large deformations compared to its thickness. Such structures are referred to as highly flexible structures in the literature (Ref. 19). As seen from the strobbed images of the wing in Fig. 2, at high frequencies the wing undergoes significant deformations. The effect of these deformations on wing aerodynamic performance needs to be modeled and quantified, which is the focus of the current research.

The geometrically exact beam and plate theories proposed by Pai (Ref. 19) is implemented in the current study. This theory accounts for the geometric nonlinearities due to large rotations, in-plane strain, initial curvature, and transverse shear deformations and encapsulates the exact shell-deformed surface (Refs. 20–23).

As shown in Fig. 1, the wing in the present study comprises of membrane and spars. The model developed is a sophisticated coupled model based on geometrically exact plate and beam theories. The membrane of the wing is modeled as highly flexible plate and the spars as beams. These independent models are coupled to form the fully developed structural model of the wing.

### Geometrically exact finite element modeling

The integral form of extended Hamilton's principle is used to determine the governing differential equation of the deformed shell and beam structure. This principle states that

$$\int_{t1}^{t2} (\delta T - \delta \Pi + \delta W_{nc})dt = 0 \tag{1}$$

where $\delta T$ is the variation in kinetic energy, $\delta \Pi$ is the variation of elastic energy, and $\delta W_{nc}$ is the nonconservative work done by external forces.

*Geometrically exact modeling.* For a naturally curved shell, three coordinate systems are needed for describing its deformation, as shown in Fig. 3. The $abc$ is a fixed global rectangular coordinate system used for reference, the $xyz$ is a fixed local orthogonal curvilinear coordinate system used to describe the undeformed shell geometry, and the $\xi\eta\zeta$ is a moving local orthogonal curvilinear coordinate system used to describe the deformed shell geometry (Ref. 23). Moreover, $i_a$, $i_b$, and $i_c$ are unit vectors along the axes $a$, $b$ and $c$, respectively; $j_1$, $j_2$, and $j_3$ are unit vectors along the axes $x$, $y$ and $z$, respectively; $i_1$, $i_2$, and $i_3$ are unit vectors along the axes $\xi$, $\eta$ and $\zeta$, respectively. It can be shown that

$$\{\mathbf{j}_{123}\} = [T^0]\{\mathbf{i}_{abc}\}, \quad \frac{d}{ds}\{\mathbf{j}_{123}\} = [K^0]\{\mathbf{i}_{abc}\} \tag{2}$$

$$[K^0] = \begin{bmatrix} \mathbf{j}_{1s}\cdot\mathbf{j}_1 & \mathbf{j}_{1s}\cdot\mathbf{j}_2 & \mathbf{j}_{1s}\cdot\mathbf{j}_3 \\ \mathbf{j}_{2s}\cdot\mathbf{j}_1 & \mathbf{j}_{2s}\cdot\mathbf{j}_2 & \mathbf{j}_{2s}\cdot\mathbf{j}_3 \\ \mathbf{j}_{3s}\cdot\mathbf{j}_1 & \mathbf{j}_{3s}\cdot\mathbf{j}_2 & \mathbf{j}_{3s}\cdot\mathbf{j}_3 \end{bmatrix} = \begin{bmatrix} 0 & k_3 & -k_2 \\ -k_3 & 0 & k_1 \\ k_2 & -k_1 & 0 \end{bmatrix} = \frac{\partial[T^0]}{\partial s}[T^0]^T \tag{3}$$

where $[T^0]$ is a known transformation matrix relating the coordinate systems $abc$ and $xyz$ and $[K^0]$ is the initial curvature matrix. $k_1$ is initial twisting curvature, and $k_2$ and $k_3$ are the initial bending curvatures.

Moreover, the deformed coordinate system $\xi\eta\zeta$ and the undeformed coordinate system $xyz$ are related to each other by the transformation matrix $[T]$ as

$$\{\mathbf{i}_{123}\} = [T]\{\mathbf{j}_{123}\} \tag{4}$$

$$[T] = \begin{bmatrix} T_{11} & T_{12} & T_{13} \\ T_{21} & T_{22} & T_{23} \\ T_{31} & T_{32} & T_{33} \end{bmatrix} = \begin{bmatrix} 1 & 0 & 0 \\ 0 & \cos\phi & \sin\phi \\ 0 & -\sin\phi & \cos\phi \end{bmatrix}$$
$$\begin{bmatrix} T_{11} & T_{12} & T_{13} \\ -T_{12} & T_{11}+T_{13}^2/(1+T_{11}) & -T_{12}T_{13}/(1+T_{11}) \\ -T_{13} & -T_{12}T_{13}/(1+T_{11}) & T_{11}+T_{13}^2/(1+T_{11}) \end{bmatrix} \tag{5}$$

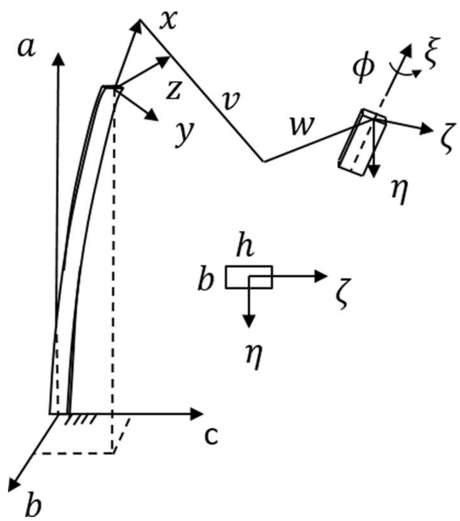


**Fig. 4. Undeformed and deformed geometries of differential reference beam with the corresponding coordinate systems (Ref. 23).**

where

$$T_{11}=\frac{1+u'-vk_3+wk_2}{1+e},\ T_{12}=\frac{v'+uk_3-wk_1}{1+e},\ T_{13}=\frac{w'-uk_2+vk_1}{1+e},$$
$$e=\sqrt{(1+u'-vk_3+wk_2)^2+(v'+uk_3-wk_1)^2+(w'-uk_2+vk_1)^2}$$

differentiating Eq. (4) with respect to $s$ and using Eq. (2) and $[T]^{-1}=[T]^T$ yields

$$\frac{d}{ds}\{\mathbf{i}_{123}\}=[K]\{\mathbf{i}_{123}\} \tag{6}$$

$$[K]=\begin{bmatrix}\mathbf{i}_{1s}\cdot\mathbf{i}_1 & \mathbf{i}_{1s}\cdot\mathbf{i}_2 & \mathbf{i}_{1s}\cdot\mathbf{i}_3\\ \mathbf{i}_{2s}\cdot\mathbf{i}_1 & \mathbf{i}_{2s}\cdot\mathbf{i}_2 & \mathbf{i}_{2s}\cdot\mathbf{i}_3\\ \mathbf{i}_{3s}\cdot\mathbf{i}_1 & \mathbf{i}_{2s}\cdot\mathbf{i}_2 & \mathbf{i}_{3s}\cdot\mathbf{i}_3\end{bmatrix}=\begin{bmatrix}0 & \rho_1 & -\rho_2\\ -\rho_3 & 0 & \rho_1\\ \rho_2 & -\rho_1 & 0\end{bmatrix}$$
$$=\frac{\partial[T]}{\partial s}[T]^T+[T][K^0][T]^T \tag{7}$$

where $\rho_1$ is the deformed twisting curvature and $\rho_2$ and $\rho_3$ are the deformed bending curvatures. Note that $\rho_i$ is not real curvature because the differentiation is with respect to the undeformed differential length $ds$, instead of the deformed length $(1+e)ds$. Using Eqs. (7), (4), and (2), one can show that

$$\rho_1=\phi'+\frac{1}{(1+e)(1+T_{11})}[T_{13}(v'+k_3u-k_1w)'-T_{12}(w'-k_2u+k_1v)']$$
$$+\ T_{11}k_1+T_{12}k_2+T_{13}k_3 \tag{8}$$

$$\rho_2=-\frac{1}{(1+e)}[T_{31}(u'+k_3v-k_2w)'-T_{12}(v'-k_2u+k_1v)'$$
$$+\,T_{33}(w'-k_2u+k_1v)']+T_{21}k_1+T_{22}k_2+T_{23}k_3 \tag{9}$$

$$\rho_3=\frac{1}{(1+e)}[T_{21}(u'-k_3v+k_2w)'-T_{22}(v'+k_3u-k_1w)'$$
$$+\,T_{23}(w'-k_2u+k_1v)']+T_{31}k_1+T_{32}k_2+T_{33}k_3 \tag{10}$$

For a naturally curved and twisted beam, as shown in Fig. 4, three coordinate systems are used to describe the deformation. The interconnectivity between these coordinates is similar to that of the plate model. Equations (2)–(10) hold true for the beam model as well.

*Finite element formulation.* For a geometrically exact beam theory, fully nonlinear stress–strain and strain-displacement relations are given by

$$\{J\}=\left[Q\right]\{B\} \tag{11}$$

where $J$ is Jaumann stress and $B$ is Jaumann strain.

$$\{J\}=\begin{Bmatrix}J_{11}\\ J_{12}\\ J_{13}\end{Bmatrix},\ \{B\}=\begin{Bmatrix}B_{11}\\ 2B_{12}\\ 2B_{13}\end{Bmatrix},\ \{Q\}=\begin{bmatrix}\mathrm{E} & 0 & 0\\ 0 & \mathrm{G} & 0\\ 0 & 0 & \mathrm{G}\end{bmatrix} \tag{12}$$

$$\{B\}=[S]\{\psi\} \tag{13}$$

with

$$\left[S\right]=\begin{bmatrix}1 & 0 & 0 & 0 & z & -y & y & z\\ 0 & 1+yk_3 & zk_3 & -z & 0 & 0 & 0 & 0\\ 0 & -yk_2 & 1-zk_2 & y & 0 & 0 & 0 & 0\end{bmatrix} \tag{14}$$

$$\{\psi\}=\{e,\ \gamma_6,\ \gamma_5,\ \rho_1-k_1,\ \rho_2-k_2,\ \rho_3-k_3,\gamma'_6,\ \ \gamma'_5\}^T \tag{15}$$

where E is Young's modulus, G is shear modulus, $\rho_i$ and $k_i$ are given in Eqs. (3) and (7).

For a geometrically exact shell theory, fully nonlinear stress–strain and strain–displacement relations are given by

$$\{J\}=[Q]\{B\} \tag{16}$$

$$\{J\}=\{J_{11},\ J_{22},\ J_{12},\ J_{23},\ J_{13}\}^T,\left[Q\right]=\begin{bmatrix}Q_{11} & Q_{12} & Q_{13} & 0 & 0\\ Q_{12} & Q_{22} & Q_{26} & 0 & 0\\ Q_{16} & Q_{26} & Q_{66} & 0 & 0\end{bmatrix} \tag{17}$$

$$\{B\}=\{B_{11},\ B_{22},\ B_{12},\ B_{23},\ B_{13}\}^T=[S]\{\psi\} \tag{18}$$

with

$$[S]=\begin{bmatrix}1&0&0&z&0&0&0&0&z&0&-k_5z&0\\ 0&1&0&0&z&0&0&z&0&0&0&k_4z\\ 0&0&1&0&0&z&z&0&0&z&-k_4z&k_5z\\ 0&0&0&0&0&0&0&0&0&0&1-k_2z&-k_{62}z\\ 0&0&0&0&0&0&0&0&0&0&-k_{61}z&1-k_1z\end{bmatrix} \tag{19}$$

$$\{\psi\}=\big\{(1+e_1)\cos\gamma_{61}-1,\ (1+e_2)\cos\gamma_{62}-1,\ (1+e_1)\sin\gamma_{61}$$
$$+(1+e_2)\sin\gamma_{62},k_1-k_1^0,\ k_2-k_2^0,\ k_6-k_6^0,\ \gamma_{4x},\ \gamma_{4y},\ \gamma_{5x},$$
$$\gamma_{5y},\ \gamma_4,\ \gamma_5\big\}^T \tag{20}$$

$$\text{where}\quad \{\psi\}=[\Psi]\{U\},\quad \Psi_{ij}=\frac{\partial\psi_i}{\partial U_j} \tag{21}$$

$$\text{beam:}\quad \{U\}=\{U_1\}=\{u,\ u',\ u'',\ v,\ v',\ v'',\ w,\ w',\ w'',\ \phi,\ \phi',\ \gamma_5,$$
$$\gamma'_5,\ \gamma_6,\ \gamma'_6\}^T \tag{22}$$

$$\text{shell:}\quad \{U\}=\{U_2\}=\{u,\ u_x,\ u_y,\ u_{xx},\ u_{xy},\ u_{yy},\ v,\ v_x,\ v_y,\ v_{xx},$$
$$v_{xy},\ v_{yy},\ w,\ w_x,\ w_y,\ w_{xx},\ w_{xy},\ w_{yy},\ \gamma_4,$$
$$\gamma_{4x},\ \gamma_{4y},\gamma_5,\ \gamma_{5x},\ \gamma_{5y}\}^T \tag{23}$$

The way that components of $U$ are approximated defines a specific finite element. Using the finite-element discretization schemes, one can discretize the displacement as

$$\text{beam}: \quad \{u, v, w, \phi, \gamma_5, \gamma_6\}^T = [N_1]\{q_1^{(j)}\} \tag{24}$$

$$\{q_1^{(j)}\} = \{u_i,\ v_i,\ w_i,\ \phi_i,\ w_i',\ v_i',\ u_i',\ \gamma_{5i},\ \gamma_{6i},\ u_k,\ v_k,\ w_k,\ \phi_k,\ w_k',\ v_k',\ u_k',\ \gamma_{5k},\ \gamma_{6k}\}^T \tag{25}$$

$$\text{shell}: \quad \{u,\ v,\ w,\ \gamma_4,\ \gamma_5\}^T = [N_2]\{q_2^{(j)}\} \tag{26}$$

$$\{q_2^{(j)}\} = \{\{q^{(l)}\}^T,\ \{q^{(l+1)}\}^T,\ \{q^{(l+2)}\}^T,\ \{q^{(l+3)}\}^T\}^T \tag{27}$$

with each node degree of freedom

$$\{q^{(l)}\} = \{u^{(l)},\ u_x^{(l)},\ u_y^{(l)},\ u_{xy}^{(l)},\ v^{(l)},\ v_x^{(l)},\ v_y^{(l)},\ v_{xy}^{(l)},\ w^{(l)},\ w_x^{(l)},\ w_y^{(l)},\ w_{xy}^{(l)},\ \gamma_4^{(l)},\ \gamma_5^{(l)}\}^T \tag{28}$$

where $q_1^{(j)}$ is the displacement vector of the $j$th beam element and $[N_1]$ is a $6\times 18$ matrix of one-dimensional shape functions, $q_2^{(j)}$ is the displacement vector of the $j$th shell element, and $[N_2]$ is a $5\times 56$ matrix of two-dimensional (2D) shape functions. Substituting Eqs. (24) and (25) in Eq. (22) and Eqs. (26) and (27) in Eq. (23) yields

$$\text{beam}: \quad U_1 = [D_1]\{q_1^{(j)}\}, \quad [D_1] = [\partial_1][N_1] \tag{29}$$

$$\text{shell}: \quad U_2 = [D_2]\{q_2^{(j)}\}, \quad [D_2] = [\partial_2][N_2] \tag{30}$$

where $[\partial_1]$, $[\partial_2]$ consisting of differential operators.

For beam, the variation of elastic energy is given by

$$\delta\Pi = \int_v \{\delta B\}^T\{J\}dV = \sum_{j=1}^{N_e}\int_{L^{(j)}}\{\delta q_1^{(j)}\}[D_1]^T[\Psi]^T[\Phi_1]\{\psi\}ds = \sum_{j=1}^{N_e}\{\delta q_1^{(j)}\}^T[K_1^{(j)}]\{q_1^{(j)}\} \tag{31}$$

where

$$[K_1^{(j)}]\{q_1^{(j)}\} = \int_{L^{(j)}}[D_1]^T[\Psi]^T[\Phi_1]\{\psi\}ds \tag{32}$$

$$[\Phi_1] = \int_A [S]^T[Q][S]dA \tag{33}$$

where $V$ is the volume, $N_e$ is the total number of elements, $L^{(j)}$ is the length of the $j$th element, and $K_1^{(j)}$ is the stiffness matrix of the $j$th beam element.

For shell, the variation of elastic energy is given by

$$\delta\Pi = \int_v \{\delta B\}^T\{J\}dV = \sum_{j=1}^{N_e}\int_{A^{(j)}}\{\delta q^{(j)}\}^T[D_2]^T[\Psi]^T[\Phi_2]\{\psi\}dA = \sum_{j=1}^{N_e}\{\delta q_2^{(j)}\}^T[K_2^{(j)}]\{q_2^{(j)}\} \tag{34}$$

where

$$[K_2^{(j)}]\{q_2^{(j)}\} = \int_{A^{(j)}}[D]^T[\Psi]^T[\Phi]\{\psi\}ds \tag{35}$$

where $N_e$ is the total number of elements, $A^{(j)}$ is the area of the $j$th element, and $K_2^{(j)}$ is the stiffness matrix of the $j$th shell element.

Therefore, for beam and shell coupling, the variation of elastic energy is given by

$$\delta\Pi = \sum_{j=1}^{N_e}\{\delta q_1^{(j)}\}^T[K_1^{(j)}]\{q_1^{(j)}\} + \sum_{k=1}^{M_e}\{\delta q_2^{(k)}\}^T[K_2^{(k)}]\{q_2^{(k)}\} \tag{36}$$

with a model including both beam and shell elements, the relation of $q_1^{(j)}$ and $q_2^{(k)}$ with global $q$ can be determined, then $[K_1^{(j)}]$ and $[K_2^{(k)}]$ would be used to form global stiffness matrix $[K]$.

The variation of kinetic energy is given by

$$\delta T = -\int_v \rho(\ddot{u}\delta u + \ddot{v}\delta v + \ddot{w}\delta w)dV \tag{37}$$

for beam and shell coupling

$$\delta T = -\int\{\delta\hat{U}\}^T[\hat{\Psi}]^T[m][\hat{\Psi}]\{\dot{\hat{U}}\}dA = -\sum_{j=1}^{N_e}\{\delta q^{(j)}\}^T[M^{(j)}]\{\ddot{q}^{(j)}\} - \sum_{k=1}^{M_e}\{\delta q^{(k)}\}^T[M^{(k)}]\{\ddot{q}^{(k)}\} \tag{38}$$

similarly, elements from $[M^{(j)}]$ and $[M^{(k)}]$ would be used to form global $[M]$ matrix.

The variation of nonconservative work due to external distributed loads is given by

$$\delta W_{nc} = \int_0^L \{\delta U\}^T\{R\}ds = \{\delta q\}^T\{R\} \tag{39}$$

where $\{R\}$ is the global nodal loading vector.

Substituting Eqs. (36), (38), and (39) into Hamilton's equation would yield the equations of motion and is given by the form of

$$[M]\{\ddot{q}\} + [C]\{q\} + [K]\{q\} = \{g\} \tag{40}$$

Similar to plate, the static problems in beam theory can be solved using the iterative method based on the modified Riks method. For dynamic problems, Eq. (40) can be solved by a direct numerical integration using the Newmark-$\beta$ method.

The Newmark-$\beta$ method is an implicit numerical integration technique used for nonlinear systems with $[M]$ and $[K]$ being displacement dependent and $\{R\}$ being displacement independent. We expand the displacement, velocity, and acceleration vectors at $t+\Delta t$ as

$$\{q\}^{t+\Delta t} = \{q\}^t + \{\Delta q\}, \quad \{\dot{q}\}^{t+\Delta t} = \{\dot{q}\}^t + \{\Delta\dot{q}\}, \quad \{\ddot{q}\}^{t+\Delta t} = \{\ddot{q}\}^t + \{\Delta\ddot{q}\} \tag{41}$$

substituting Eq. (41) into Eq. (40) yields

$$[\hat{M}]^t\{\ddot{q}\} + [\hat{C}]^t\{q\} + [\hat{K}]^t\{q\} = \{g\}^t \tag{42}$$

where $[\hat{M}]$, $[\hat{C}]$, and $[\hat{K}]$ are the tangent mass, damping, and stiffness matrices at time $t$, and

$$\{g\}^t = (\{R\}^{t+\Delta t} - [M]\{\ddot{q}\} - [C]\{\dot{q}\} - [K]\{q\}) \tag{43}$$

Assume the velocity vector $\{\dot{q}\}^{t+\Delta t}$ and displacement vector $\{q\}^{t+\Delta t}$ to be

$$\{\dot{q}\}^{t+\Delta t} = \{\dot{q}\}^t + [(1-\alpha)\{\ddot{q}\}^t + \alpha\{\ddot{q}\}^{t+\Delta t})]\Delta t \tag{44}$$

$$\{q\}^{t+\Delta t} = \{q\}^t + \{\dot{q}\}^t\Delta t + \left[\left(\frac{1}{2} - \beta)\{\ddot{q}\}^t + \beta\{\ddot{q}\}^{t+\Delta t}\right)\right]\Delta t^2 \tag{45}$$

solving from Eq. (45) for $\{\ddot{q}\}^{t+\Delta t}$ and substitute into Eq. (44) gives expression of $\{\Delta\ddot{q}\}$ and $\{\Delta\dot{q}\}$, substituting the expression into Eq. (42)

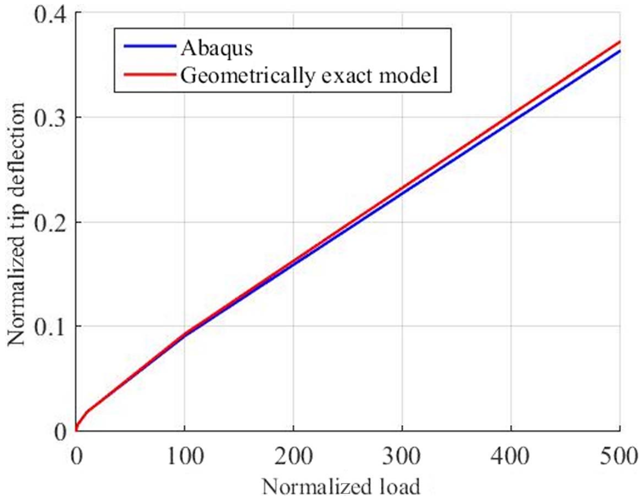


**Fig. 5. Effect of varying pressure on the deflection.**

yields

$$[\tilde{K}]^t\{\Delta q\} = \{\tilde{R}\}^t \tag{46}$$

where

$$[\tilde{K}]^t = [\hat{K}]^t + \frac{1}{\beta \Delta t^2}[\hat{M}]^t \tag{47}$$

$$\tilde{R}^t = \left(\{\hat{R}\}^{t+\Delta t} - [\hat{M}]\{\ddot{q}\} - [\hat{K}]\{q\}\right)_{\{q\}=\{q\}^t} + [\hat{M}]^t\left(\frac{1}{2\beta}\{\ddot{q}\}^t + \frac{1}{\beta \delta t}\{\dot{q}\}^t\right) \tag{48}$$

One can solve Eq. (46) for $\Delta q$ and substitute into other equations to obtain $\{\Delta q\}^{t+\Delta t}$, $\{\Delta \dot{q}\}^{t+\Delta t}$, and $\{\Delta \ddot{q}\}^{t+\Delta t}$.

## Shell and Beam Model Simulation

### Shell model

The geometrically exact shell theory was implemented using 2D finite elements on a Delrin plate of dimension 0.254 × 0.254 × 0.0007 m. The plate is pinned at two adjacent edges, and varying pressure is applied on the plate.

The study has been carried out to understand and validate the structural model. The deflections of the plate when subjected to static loading are obtained. The deflection corresponding to the loading with varying load factor is shown in Fig. 5. The tip deflection of the plate corresponding to varying load values is plotted and compared with that obtained from Abaqus FEA software. It shows that the deflections predicted by the current structural model are in good agreement with that of the high-fidelity commercial finite element software even for very large deflections. It could thus be deduced from these comparisons that the present shell model is capable of predicting the deflection of highly flexible structures such as the flapping wing in the current study.

### Beam model

The geometrically exact beam model hence developed has also been validated by comparing with the results predicted by Abaqus FEA software. A particular case of static deflections of a cantilever beam (0.125 inch × 0.5 inch × 20 inch) held at an angle of 15° from vertical due to application of distributed load along the elastic axis was considered.

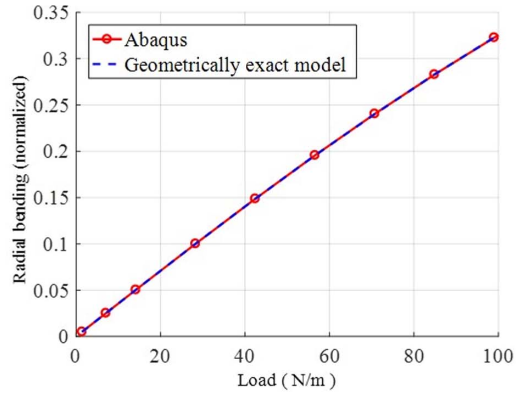


**(a) Comparison of tip radial bending**

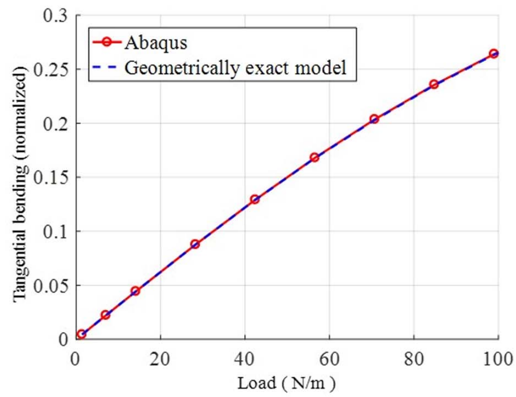


**(b) Comparison of tip tangential bending**

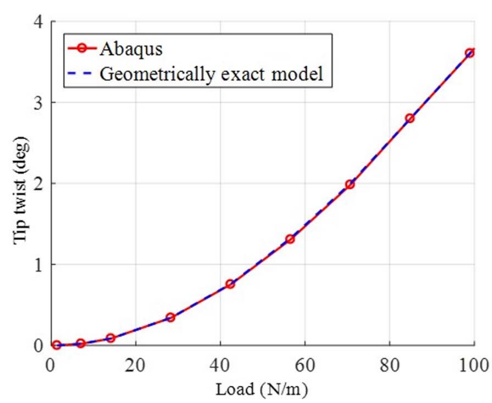


**(c) Comparison of tip twist**

**Fig. 6. Comparison of tip deflection for a cantilever beam with uniform load applied at the elastic axis at 15° angle.**

Figures 6(a)–6(c) show comparison of tip radial bending, tip tangential bending and tip twist, respectively, with increasing distributed vertical load (along the $x$-axis) on the beam. Predictions of bending deflections and twists by geometrically exact beam model are accurate even for large bending and torsional deflections as shown in these figures. Further validation tests were carried out for beams of different boundary conditions and were observed to match with the results from Abaqus (Ref. 24).

These systematic study reveals the level of accuracy of the geometrically exact beam and plate models to capture the large nonlinear deflections.

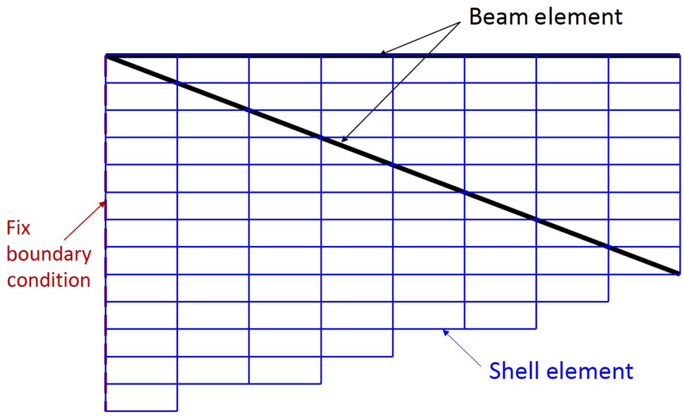


**Fig. 7. Test model**

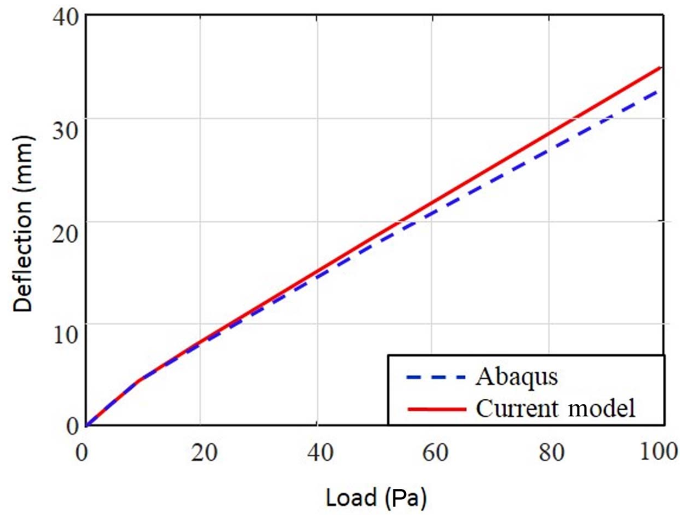


**Fig. 8. Tip deflection comparison between the present geometrically exact model and Abaqus.**

**Beam–shell coupling**

As shown in Fig. 1, the bioinspired flapping wing design has the wing structure comprises of carbon fiber spars (modeled as beams) and foam membrane (modeled as shell). So it is necessary to develop a structural model that is capable of beam–shell coupled analysis. Figure 7 shows a cantilevered structure modeled with both beam and shell elements. The tip deflection corresponding to the loading with varying load factor is compared with the Abaqus simulation result, as shown in Fig. 8. It shows good agreement between Abaqus and present model predictions.

## Aerodynamic Model

The aerodynamic analysis is a modified lifting-line solution including unsteady models (Refs. 25,26). Fig. 9(a) shows illustration of an idealized conception of the vortex structure of flapping wing, and Fig. 9(b) is a more detailed vortex lattice description of the current model. In this approach, the vortex sheet is comprised of vorticity vectors aligned normal and parallel to the trailing edge of the wing. The strength of the former component (the trailed vorticity) is related to the spanwise gradient of lift (circulation, $\Gamma$) on the blade (i.e., to $\partial\Gamma/\partial r$), whereas the latter component (the shed vorticity) is related to the time rate of change of lift on the wing (i.e., $\partial\Gamma/\partial t$). In the current aerodynamic model, trailed vorticity is modeled by the wake vortex model and shed vorticity effect is modeled as unsteady effects.

Physically, the aerodynamic loading on the wing is biased towards the tip. This leads to high spanwise gradient of vorticity at tip of the wing, thus the trailed vorticity gets higher in overall strength, which causes significantly high induced velocities at tip area, resembling the effect of strong tip vortex as shown in Fig. 9(a).

In the present model, it is assumed that the aerodynamic forces acting on a flapping wing can be broken down into a number of components, which can be added together to get the total force (Ref. 10). The following components contribute to total aerodynamic force on the wing: leading-edge vortex, trailed wake vortex, and unsteady effects due to starting vortex and shed wake.

*Lifting airfoil model.* The wing is divided into $N$ spanwise sections. Based on thin airfoil theory, vortex distribution $\gamma(x)$ on the each spanwise section can be obtained by solving the integral equation of the zero through-flow boundary condition.

$$\frac{1}{2\pi}\int_0^c \frac{\gamma(\xi)}{x-\xi}d\xi = V_n - V_p\frac{d\omega}{dx} + \dot{\theta}(x-ac) - \dot{\omega}(x) \tag{49}$$

where $V_n$ is the flow velocity normal to airfoil, $V_p$ is the velocity along airfoil direction, and $\omega$ is out-of-plane deflection of the airfoil. Since both the normal and parallel velocities are considered separately in the equation, there is no small angle of attack assumption involved. To solve this equation, the classical approach is to approximate $\gamma(x)$ by a trigonometric expansion.

$$x = \frac{c}{2}(1-\cos\phi) \tag{50}$$

The airfoil leading edge corresponds to $x = 0$ ($\phi = 0$), and the trailing edge is at $x = c$ ($\phi = \pi$). To satisfy the Kutta condition at the trailing edge, the expression of circulation distribution $\gamma$ can be written as a Fourier series (Ref. 25)

$$\gamma(\phi) = 2V_\infty\left(A_0\frac{1+\cos\phi}{\sin\phi} + \sum_{n=1}^{\infty} A_n \sin\phi\right) \tag{51}$$

where $V_\infty$ is the total free-stream flow velocity. The Fourier series coefficients can be determined as

$$A_0 = \frac{V_n}{V_\infty} + \frac{c\dot{\theta}}{V_\infty}\left(\frac{1}{2}-a\right) - \frac{V_p}{\pi V_\infty}\int_0^\pi \frac{\partial\omega}{\partial x}d\phi \tag{52}$$

$$A_1 = \frac{1}{2}\frac{c\dot{\theta}}{V_\infty} - \frac{2V_p}{\pi V_\infty}\int_0^\pi \frac{\partial\omega}{\partial x}\cos\phi d\phi \tag{53}$$

The total circulation can be obtained by integrating $\gamma(\Phi)$ along the chord,

$$\Gamma(t) = \pi V_\infty c\left(A_0(t) + \frac{A_1(t)}{2}\right) \tag{54}$$

This circulation distribution is used as an initial condition for the first flap cycle.

*Wake vortex model.* For a vortex segment with ends at point 1 and point 2, the induced velocity at an arbitrary point P can be obtained by

$$\mathbf{q}_{1,2} = \frac{\Gamma}{4\pi}\frac{\mathbf{r}_1\times\mathbf{r}_2}{|\mathbf{r}_1\times\mathbf{r}_2|^2}\mathbf{r}_0\cdot\left(\frac{\mathbf{r}_1}{r_1}-\frac{\mathbf{r}_2}{r_2}\right) \tag{55}$$

where $\mathbf{r}_1$, $\mathbf{r}_1$ are vectors connecting point 1 to point P and point 2 to point P, respectively.

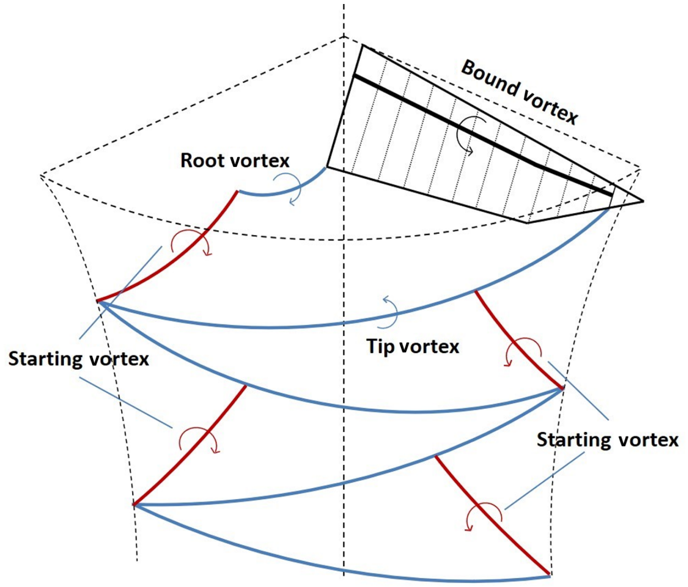


**(a) An idealized conception of the vortex structure of flapping wing**

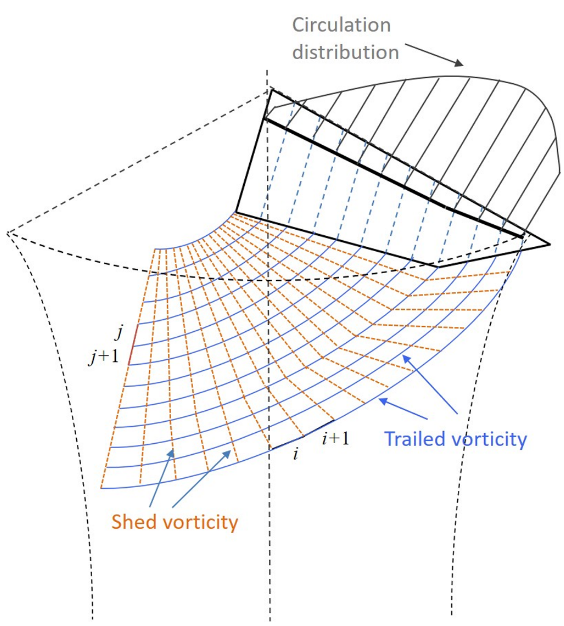


**(b) Schematic showing wake vortex structure of half cycle**

**Fig. 9. Schematic showing wake vortex of flapping wing.**

For a system comprising of wing spanwise elements and wake vortex segments, we define a general expression $\mathbf{q}_{ij}^{b}$ that represents induced velocity at collocation point $i$ by the circulation at section $j$, and $\mathbf{q}_i^{v}$ represents induced velocity at collocation point $i$ by all wake vortex segments. For example, no normal flow across the wing boundary condition can be rewritten for the first collocation point as

$$\left[\mathbf{q}_{11}^{b} + \mathbf{q}_{12}^{b} + \cdots + \mathbf{q}_{1N}^{b} + \mathbf{q}_1^{v} + \mathbf{Q}_\infty\right] \cdot \mathbf{n}_1 = 0 \tag{56}$$

where $\mathbf{Q}_\infty$ is free-stream velocity. $\mathbf{q}_1^{v}$ is induced velocity at collocation point 1 by trailed wake vortex segments. $\mathbf{q}_1^{v}$ can be computed using Eq. (59). $\mathbf{q}_{ij}^{b}$ can be written in the form of influence coefficients multiplied by corresponding bound circulation strength. Eq. (56) can be written as

$$\left[a_{11}\Gamma_1^{b} + a_{12}\Gamma_2^{b} + \cdots + a_{1N}\Gamma_N^{b} + \mathbf{q}_1^{v} + \mathbf{Q}_\infty\right] \cdot \mathbf{n}_1 = 0 \tag{57}$$

where $\Gamma_1^{b}, \ldots, \Gamma_N^{b}$ are bound circulation strengths. The influence coefficients are computed by $a_{ij} = \mathbf{q}_{ij}^{b} \cdot \mathbf{n}_i$ and $\mathbf{q}_{ij}^{b}$ is computed with unit bound circulation strength $\Gamma_j^{b}$. Utilizing the same procedure for each of the collocation points results in the following set of equations:

$$\begin{bmatrix} a_{11} & a_{12} & a_{13} & \ldots & \ldots & a_{1N} \\ a_{21} & a_{22} & a_{23} & \ldots & \ldots & a_{2N} \\ a_{31} & a_{32} & a_{33} & \ldots & \ldots & a_{3N} \\ \ldots & \ldots & \ldots & \ldots & \ldots & \ldots \\ \ldots & \ldots & \ldots & \ldots & \ldots & \ldots \\ a_{N1} & a_{N2} & a_{N3} & \ldots & \ldots & a_{NN} \end{bmatrix} \begin{pmatrix} \Gamma_1^{b} \\ \Gamma_2^{b} \\ \Gamma_3^{b} \\ \ldots \\ \ldots \\ \Gamma_N^{b} \end{pmatrix} = \begin{pmatrix} -\left(\mathbf{Q}_\infty + \mathbf{q}_1^{v}\right) \cdot \mathbf{n}_1 \\ -\left(\mathbf{Q}_\infty + \mathbf{q}_2^{v}\right) \cdot \mathbf{n}_2 \\ -\left(\mathbf{Q}_\infty + \mathbf{q}_2^{v}\right) \cdot \mathbf{n}_3 \\ \ldots \\ \ldots \\ -\left(\mathbf{Q}_\infty + \mathbf{q}_2^{v}\right) \cdot \mathbf{n}_N \end{pmatrix} \tag{58}$$

In these equations, the values of all the terms on the right-hand side are known. Equation (58) can be solved using standard matrix methods to obtain the bound circulation strengths.

The velocity induced by trailed vortex segments at the $i_{\mathrm{th}}$ collocation point ($q_i^{v}$) can be calculated as shown below:

$$\begin{pmatrix} \mathbf{q}_1^{v} \\ \mathbf{q}_2^{v} \\ \mathbf{q}_3^{v} \\ \ldots \\ \ldots \\ \mathbf{q}_N^{v} \end{pmatrix} = \begin{bmatrix} b_{11} & b_{12} & b_{13} & \ldots & \ldots & b_{1M} \\ b_{21} & b_{22} & b_{23} & \ldots & \ldots & b_{2M} \\ b_{31} & b_{32} & b_{33} & \ldots & \ldots & b_{3M} \\ \ldots & \ldots & \ldots & \ldots & \ldots & \ldots \\ \ldots & \ldots & \ldots & \ldots & \ldots & \ldots \\ b_{N1} & b_{N2} & b_{N3} & \ldots & \ldots & b_{NM} \end{bmatrix} \begin{pmatrix} \Gamma_1^{v} \\ \Gamma_2^{v} \\ \Gamma_3^{v} \\ \ldots \\ \ldots \\ \Gamma_M^{v} \end{pmatrix} \tag{59}$$

$\Gamma_i^{v}$ is the $i_{\mathrm{th}}$ trailed wake vortex segment with its strength the same as corresponding bound circulation at the time it was shed. The induced velocity is used to compute effective angle of attack at each wing spanwise section.

The wake is force free and the wake-induced convection of each wake vortex segment can be calculated using the Biot–Savart law, using Eq. (55).

*Leading-edge suction.* In Polhamus leading edge suction theory, the suction force generated by the presence of a leading-edge vortex on top of the wing was modeled by assuming that at high angle of attack, the leading edge suction force on the airfoil is rotated by 90 deg and acts in the same way as the suction force that would be generated by the presence of a vortex on the top of the wing. The normal force is given by

$$F_n^{\mathrm{pol}}(t) = \rho\Gamma(t)V_h(t)\sin(\alpha) \tag{60}$$

*Unsteady effects.* The unsteady effects due to shed vorticity are captured by the buildup of circulation over airfoil, accounted for using the Wagner function, which is the solution for the indicial lift on a thin airfoil undergoing step change in the angle of attack in incompressible flow.

$$F_v^{c}(t) = \rho V_h(0)\Gamma(0)\phi_\omega(t) + \rho V_h(t)\int_0^t \frac{d\Gamma}{d\sigma}\phi_\omega(t-\sigma)d\sigma \tag{61}$$

$$F_h^{c}(t) = \rho V_v(0)\Gamma(0)\phi_\omega(t) + \rho V_v(t)\int_0^t \frac{d\Gamma}{d\sigma}\phi_\omega(t-\sigma)d\sigma \tag{62}$$

The effect of the shed wake from previous flapping strokes was obtained using the Kussner function. The Kussner function can be used with the Duhamel superposition integral to obtain the lift response to an arbitrary vertical upwash field.

A schematic of the aerodynamic model simulation is shown in Fig. 10.

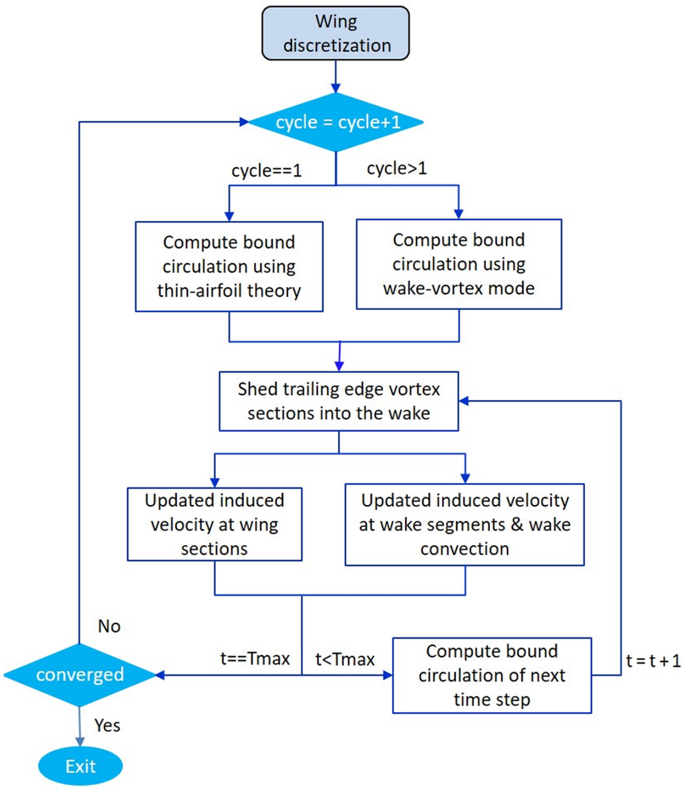


**Fig. 10. Scheme of the aerodynamic model.**

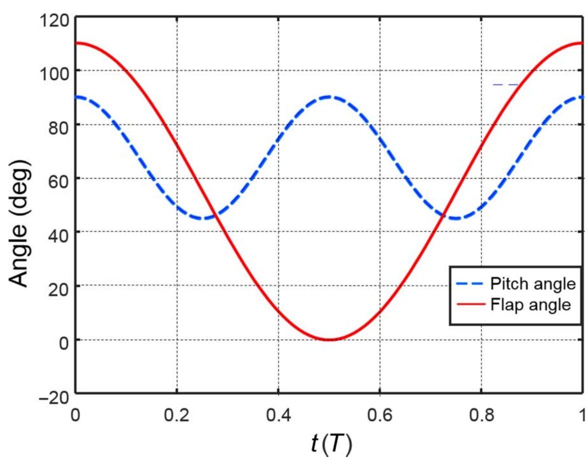


**Fig. 11. Kinematics with time history of flap and pitch angles.**

### Aerodynamic model validation

To validate the aerodynamic model, the lift predictions were compared with in-house CFD simulations of a rigid flapping wing. The CFD simulation is conducted using a compressible unsteady Reynolds averaged Navier Stokes solver (Ref. 27). The rigid wing has the same planform as the wing of hummingbird-inspired MAV as shown in Fig. 1. Three groups of cases were simulated with three kinematics parameters altered for each group: flap frequency, flap amplitude, and midstroke pitch angle. A typical kinematics is shown in Fig. 11, with a flap frequency of 20 Hz, flap amplitude of 55 deg, and midstroke pitch angle 45 deg.

Lift force time histories for each of the three groups of cases are shown in Figs. 12, 13, and 14, respectively. It is apparent that there is a 10–20% difference in the magnitude of instantaneous lift force between the CFD simulations and the current aerodynamic model. However, this level of discrepancy could be acceptable considering the fact that the current analysis is based on potential flow assumptions and could generate these results at orders of magnitude lower computational cost as compared to CFD. From these figures, it is also observed that phase shift of lift force peak between two simulations is minimal.

The time-averaged lift comparison between CFD simulation and current model for the nine different kinematics discussed above is shown in Fig. 15. For most cases, the discrepancy is lower than 10%. Since the objective is to use the present model in design codes, trim analysis, flight dynamic simulations, etc., good prediction of cycle-averaged forces is more important than the time history.

## Aeroelastic Analysis

For highly flexible flapping wings, such as the one investigated in the present study, structural deformation and aerodynamic forces are strongly coupled. Nonlinear fluid–structure interaction makes gauging the performance of such a system extremely difficult. In the present model, in order to capture the large nonlinear wing deflection, geometrically exact structural model of the wing is coupled with the unsteady aerodynamic model to perform an aeroelastic analysis.

The aeroelastic coupled solution is based on a time-domain partitioned solution process, in which the nonlinear partial differential equations modeling the dynamic behavior of structure and aerodynamic equations are solved independently with boundary information (aerodynamic loads and structural displacements) being shared between each other alternately. A schematic of such a framework is shown in Fig. 16.

The coupling algorithm adopted in this work is an explicit approach, where the solution is time-marched, and boundary information is updated on a cycle-by-cycle basis. The bilinear interpolation algorithm is used for information exchange between the two meshes.

The convergence criterion is verified for the wing tip out-of-plane displacement. At the start of a coupled aeroelastic simulation, the structural model is run for several cycles to obtain the wing deflection under only inertial load. The deflected wing shape is input into the aerodynamic solver, from which the airfoil section, angle of attack, and camber line are calculated, and this information is used in the aerodynamic model to compute aerodynamic pressure distribution. The pressure distribution on each element is interpolated back to the structural mesh to update the loading on the structural model. This exchange of information is continued in a loop until the predetermined convergence criterion is satisfied.

### Aeroelastic model validation

A state-of-art flapping wing test rig was designed and built to measure the time history of lift forces acting on a flexible wing, and the DIC technique is used to obtain the deflected wing shape at any instant in the flap cycle (Ref. 18).

Figure 17 shows the robotic hummingbird wing mounted on the flapping rig. The wing has a length of 120 mm and root chord of 50 mm. This wing design is used in the aeroelastic analysis. As shown in the figure, the stiff frame of the wing was made out of carbon fiber, whereas the wing surface is made out of flexible polyethylene foam which is 1/32 inch thick. The prescribed kinematics of the wing is pure flapping, and the pitching would be obtained passively utilizing elastic wing deflections.

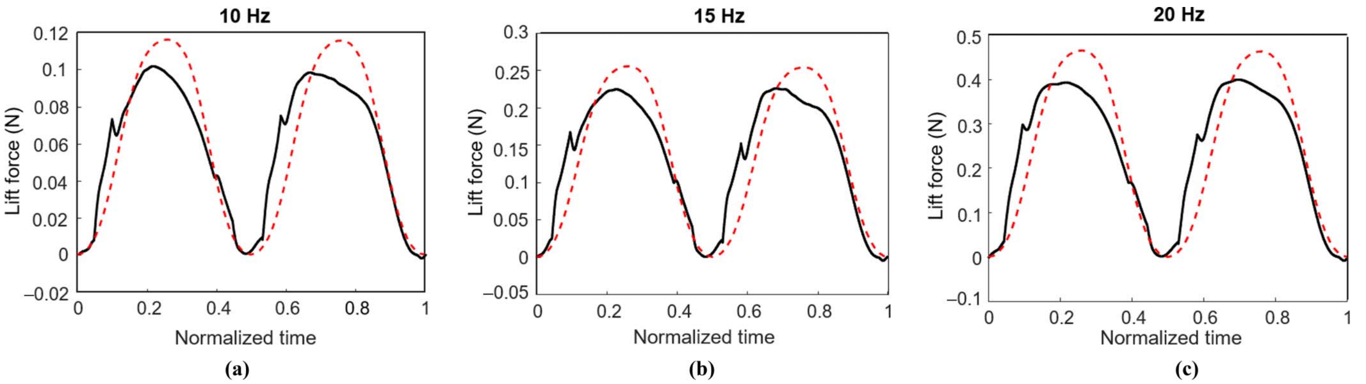


Simulation with different flap frequencies. Flap amplitude: 55°, midstroke pitch angle: 45°.
Black line: CFD simulation; red dotted line: current model.

**Fig. 12. Simulation cases with different flap frequencies.**

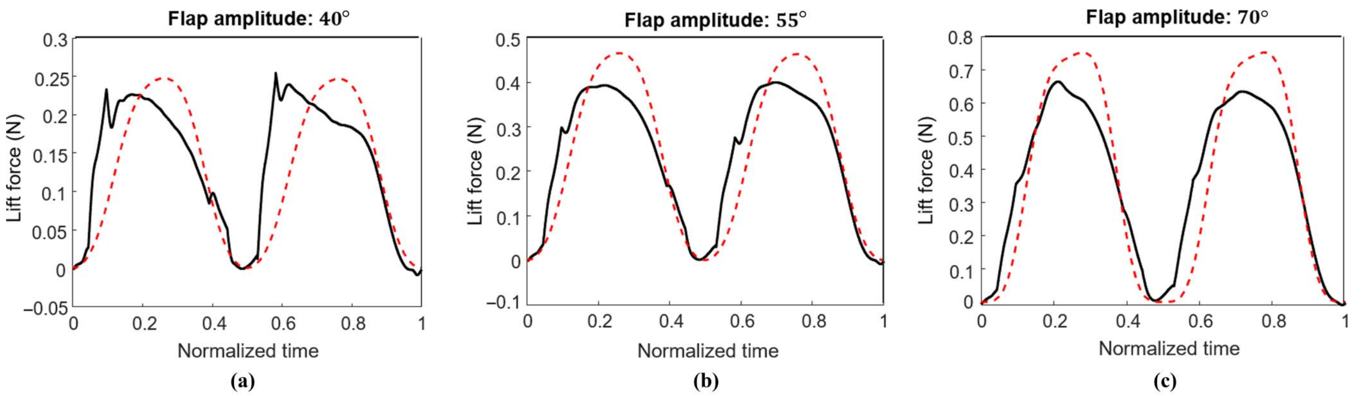


Simulation with different flap amplitude. Flap frequency: 20 Hz, midstroke pitch angle: 45°.
Black line: CFD simulation; red dotted line: current model.

**Fig. 13. Simulation cases with different flap amplitudes.**

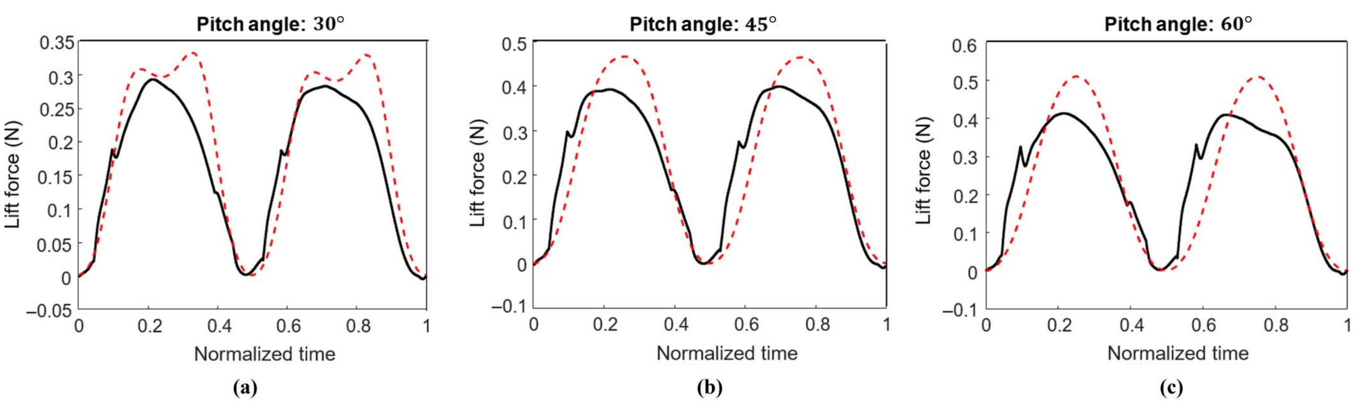


Simulation with different midstroke pitch angle. Flap frequency: 20 Hz, flap amplitude: 55°.
Black line: CFD simulation; red dotted line: current model.

**Fig. 14. Simulation cases with different midstroke pitch angles.**

The wing flapping kinematics is approximated as $\beta = 55^\circ \sin(\omega t - \pi/2)$. A strain-gaged beam-based miniature force balance was installed at the wing root to measure the instantaneous vertical forces acting on the wing during flapping. Inertial force in the vertical direction computed using dynamic wing deflection measurements was subtracted from the total measured vertical force to obtain time history of lift produced by the wing.

For the structural model, the wing was discretized using a finite element mesh. As shown in Fig. 18, shell and beam elements were used to model different parts of the wing structure and different material

| Flap frequency | | 10 Hz | 15 Hz | 20 Hz |
|---|---|---|---|---|
| Average lift force (N) | CFD | 0.0590 | 0.1338 | 0.2363 |
| | Current model | 0.0594 | 0.1324 | 0.2377 |

**(a)**

| Flap amplitude | | 40° | 55° | 70° |
|---|---|---|---|---|
| Average lift force (N) | CFD | 0.1385 | 0.2363 | 0.3587 |
| | Current model | 0.1258 | 0.2377 | 0.3847 |

**(b)**

| Midstroke pitch angle | | 30° | 45° | 60° |
|---|---|---|---|---|
| Average lift force (N) | CFD | 0.1679 | 0.2363 | 0.2449 |
| | Current model | 0.1921 | 0.2377 | 0.2432 |

**(c)**

**Fig. 15. Average lift force comparison for different cases.**

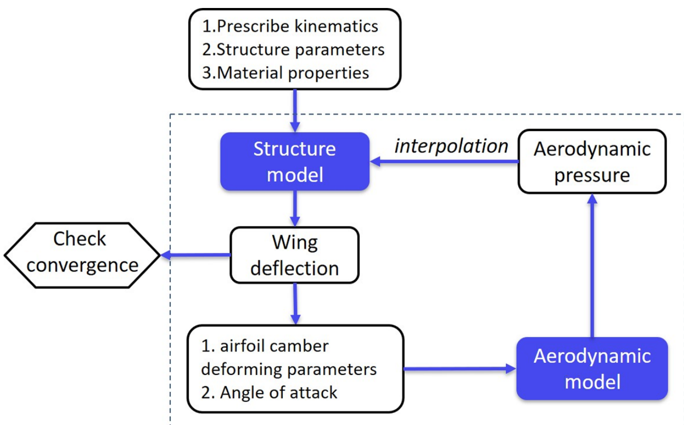


**Fig. 16. Implementation of the aerostructure coupling in the aeroelastic model.**

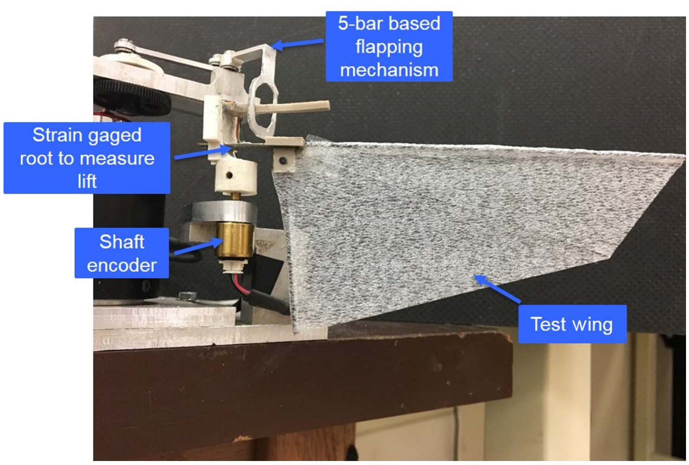


**Fig. 17. Experiment setup.**

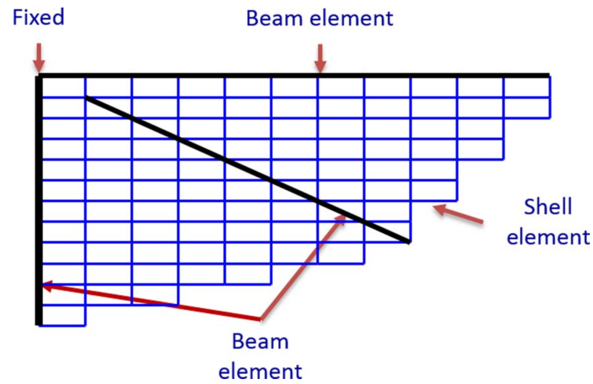


**Fig. 18. Finite element model of the wing.**

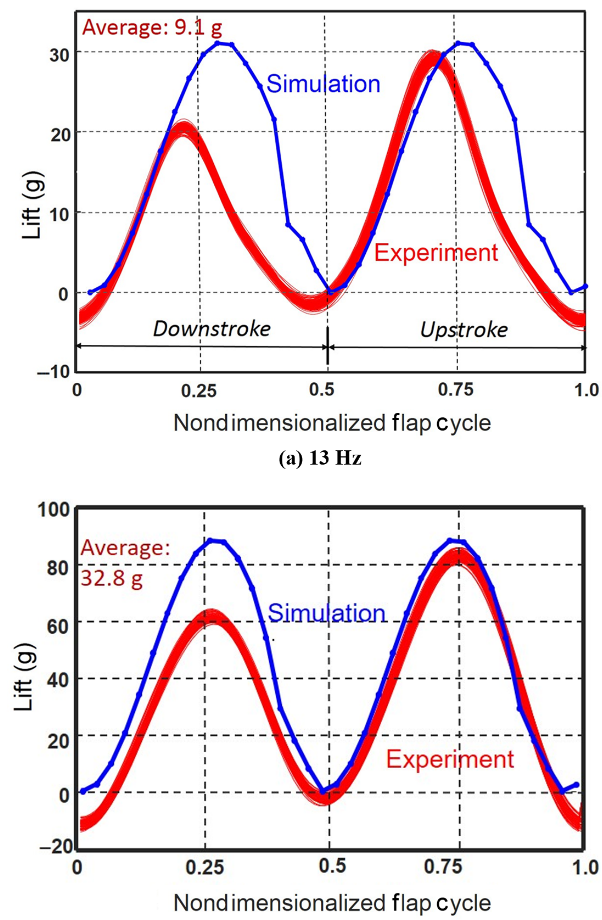


**(a) 13 Hz**

**(b) 20 Hz**

**Fig. 19. Lift force comparison.**

properties were set to the corresponding elements. At the root of the wing, a fixed boundary condition is set to the nodes.

Two cases with different flap frequencies, 13 and 20 Hz were simulated. Twenty hertz is the frequency at which the robot hummingbird operates in hover. Simulation results were compared with experimental data in terms of time history of lift force and 2D deflected airfoil shapes at two different spanwise locations and varying flap locations.

Figure 19 shows comparison of lift time history between simulation and experimental data from (Ref. 18) for flapping frequencies of 13 and

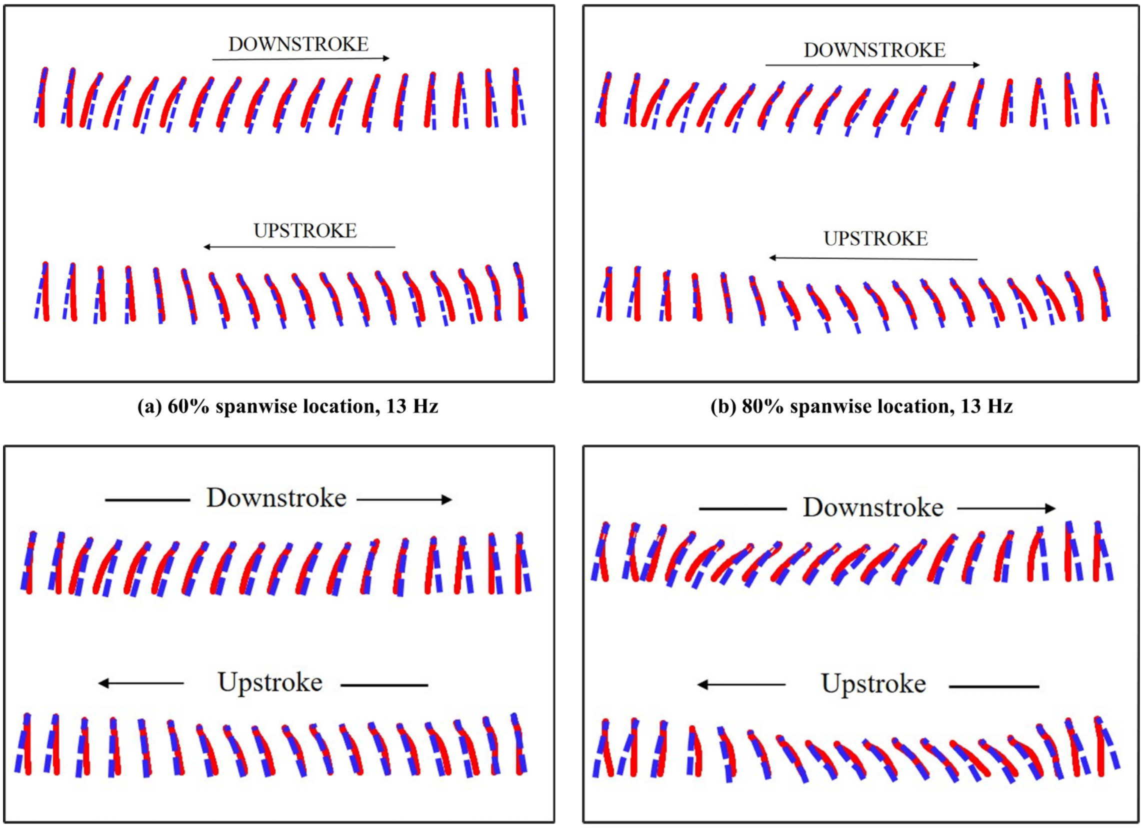


**(a) 60% spanwise location, 13 Hz** **(b) 80% spanwise location, 13 Hz**

**(c) 60% spanwise location, 20 Hz** **(d) 80% spanwise location, 20 Hz**

**Fig. 20. Airfoil shape at different instants during the flap cycle (continuous line: experiment, dotted line: simulation).**

20 Hz. Overall, there is a good correlation between the present analysis and the experiment.

For the 13-Hz case (Fig. 19), the wing produces average lift of about 9.1 g and a peak thrust of approximately 32 g in the experiment. The force predicted by CFD is symmetric between upstroke and downstroke. In both cases, the force peak occurs around midstroke, when wing attains the highest velocity. Then force drops quickly while wing speed drops and inertial force increases. Deceleration of the wing increases the angle of attack. It shows the peak of lift force occurs approximately at the same instant for both experiment and simulation.

The key difference between the predictions and test data is that the lift peaks in the experiment is not symmetric and lower than the analysis during the upstroke. Plausible reasons that attribute to the differences between experiment and simulation are listed here. (1) The membrane in wing is made out of polyethylene foam. In the simulation, it was assumed to be isotropic. It was observed that the foam has a large porosity volume fraction, and the material properties could have been estimated inaccurately. (2) The experimental data show that there is a considerable difference in forces between the downstroke and upstroke of the wing. This might be due to the fact that in experiment, the foam is glued to only one side of the frame. This makes bending stiffness not symmetric in two directions, producing dissimilar deflected wing shape (both angle of attack and camber) during upstroke and downstroke.

For the 20-Hz case from Fig. 19, it can be seen that the simulation result is quite close to experimental data. One reason is that experiment data itself show better symmetry between downstroke and upstroke compared to the 13-Hz result.

For the two flapping frequencies, the deflected airfoil shape at 60% and 80% spanwise location was extracted from the experimental data. These shapes were compared with those obtained from simulation as shown in Fig. 20. For both 13 and 20 Hz cases, except for end of stroke period, simulation result correlates well with experimental data. There is good agreement in both passive sectional pitch and camber. At stroke ends, inertial loads dominate and wing deflection changes rapidly, making it difficult to predict deformation accurately.

## Trim Analysis for the Vehicle in Hover

Once the aeroelastic model was systematically validated, it was used for the trim analysis of the robotic hummingbird (Fig. 1) in a hovering state. Trim analysis involves calculation of flapping wing controls, vehicle orientation, and wing response such that the vehicle trim equations and the wing response equations are satisfied simultaneously.

Trim equations are basically equilibrium equations that are obtained by balancing all the forces (vertical, longitudinal, and lateral) and moments (roll, pitch, and yaw) on the vehicle. This requires that the solution of the flapping equations converges to a periodic solution and the wing forces satisfy the vehicle trim equations, which implies that the resultant forces and moments on the vehicle, averaged over one flapping cycle, are zero.

A hovering vehicle has six degrees of freedom and thus requires six vehicle trim equations. For the present study, longitudinal direction, lateral direction, and yaw equilibrium are assumed to be automatically satisfied because of the same stroke amplitude for left and right wings

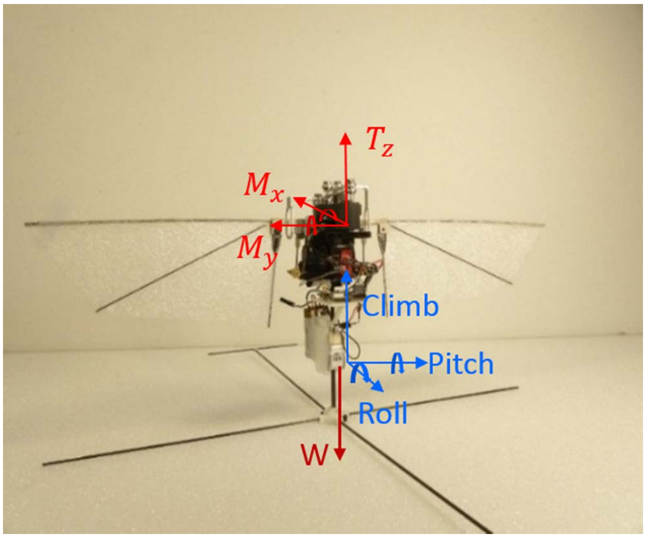


**Fig. 21. Forces and moments on the MAV.**

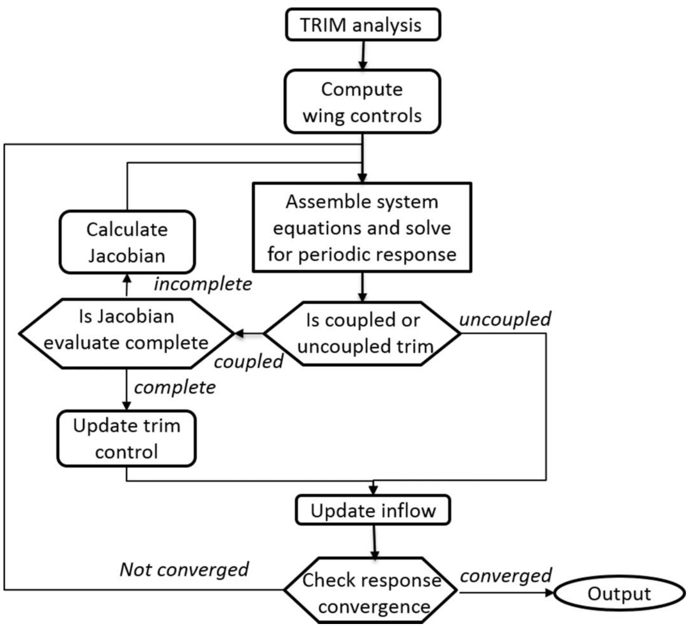


**Fig. 22. Flowchart showing the trim analysis.**

and zero stroke-plane tilt, leaving the three trim equations given below. The forces and moments acting on the MAV in this scenario are shown in Fig. 21.

$$\text{Vertical force:} \quad F_1 = T_L + T_R - W \tag{63}$$

$$\text{Pitching moment:} \quad F_2 = T_L \times r \times \sin\phi_L + T_R \times r \times \sin\phi_R - W \times x_{cg} \tag{64}$$

$$\text{Rolling moment:} \quad F_3 = T_L \times r \times \cos\phi_L - T_R \times r \times \cos\phi_R - W \times y_{cg} \tag{65}$$

where $T_L$ and $T_R$ are cycle-averaged thrust of left and right wings. $\phi_L$ and $\phi_R$ are midstroke angle of left and right wings, and $x_{cg}$ and $y_{cg}$ refer to the vehicle center of gravity offset measured from the geometric center of the vehicle. $F_1$, $F_2$, $F_3$ are residuals of the trim equations.

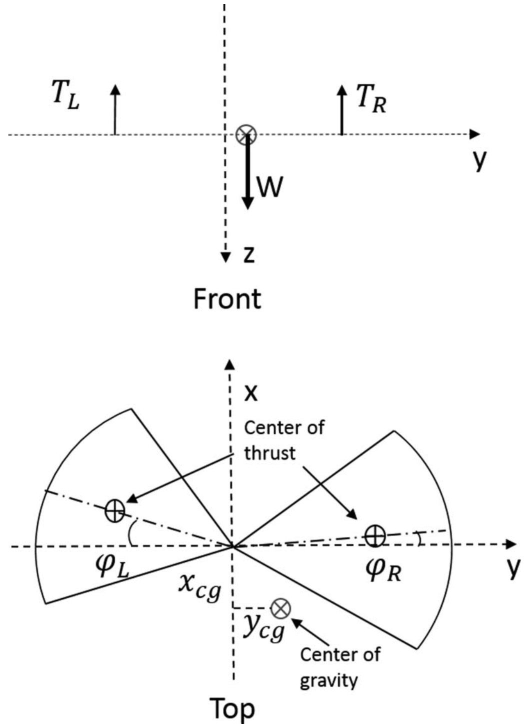


**Fig. 23. MAV configuration used for the trim case.**

An iterative control update scheme, in conjunction with wing response solution, is used to predict the control values that satisfy wing response and vehicle trim equations. The nonlinear vehicle equilibrium equations are linearized about the trim controls using a Taylor's series expansion,

$$F(\theta_i + \Delta\theta_i) = F(\theta_i) + \frac{\partial F}{\partial \theta}|_{\theta=\theta_0}\Delta\theta_i = 0, \tag{66}$$

$F$ corresponds to the residuals in the vehicle trim equation given by $F_1$, $F_2$. Rearranging Eq. (66) yields

$$\Delta\theta_i = -\left[\frac{\partial F}{\partial \theta}\right]^{-1}_{\theta=\theta_0} F(\theta_i). \tag{67}$$

For a converged solution, $\Delta\theta$ and $F$ are zero. The controls are updated as follows:

$$\theta_{i+1} = \theta_i + \Delta\theta_i. \tag{68}$$

The trim Jacobian matrix, $\partial F/\partial\theta$, is calculated using a forward finite difference approximation at $\theta = \theta_0$, and it is generally held constant through the analysis to save computation time.

To compute the Jacobian, the controls are perturbed individually. Loads computed are then input to the vehicle trim equations, and the change in the residuals, $F$, is computed using a finite difference approximation:

$$\frac{\partial F}{\partial \theta}|_{\theta=\theta_0}\Delta\theta_i = 0. \tag{69}$$

where $\Delta\theta_i$ are small control perturbations, which can be chosen to be around 5% of the original values.

### Coupled trim simulation

Coupled trim analysis is based on the aeroelastic model of the flapping wing. Since the wing flapping frequency is much higher than the

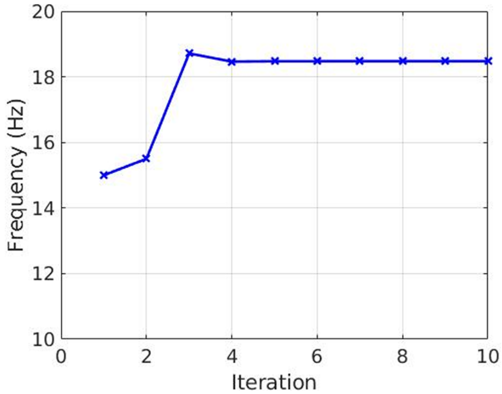


**(a) Frequency convergence**

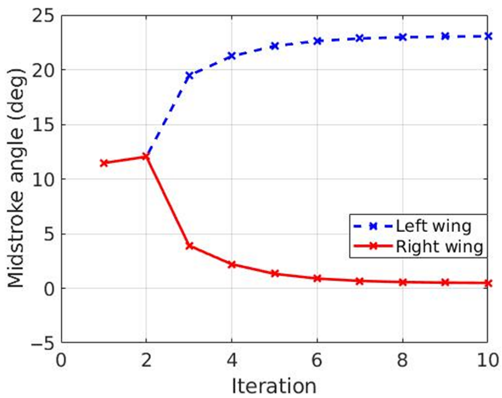


**(b) Midstroke angle convergence**

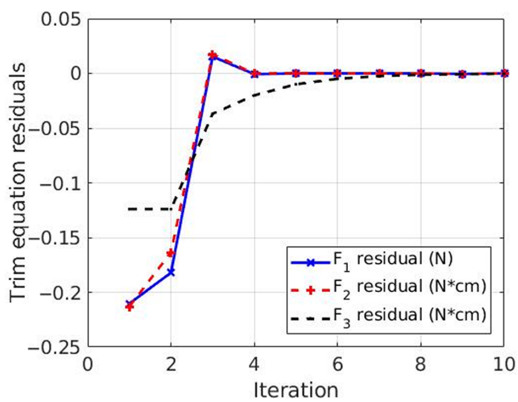


**(c) Trim equation residual**

**Fig. 24. Control parameters convergence for the trim analysis.**

frequencies of the vehicle rigid body modes, only cycle-averaged forces are used for the trim analysis. A flowchart of the coupled trim procedure is shown in Fig. 22.

Configuration of the vehicle is shown as Fig. 23. The $x$ direction c.g. offset $x_{cg}$ is 10 mm, and the $y$ direction c.g. offset $y_{cg}$ is 2 mm. These two values are used as parameters in trim equations. The three control inputs chosen here are midstroke angle (or mean stroke angle) of the left wing $\phi_L$, midstroke angle of the right wing $\phi_R$, and flap frequency $f$. The Jacobian matrix is given by

$$\frac{\partial F}{\partial \theta} = \begin{bmatrix} \frac{\partial F_1}{\partial \phi_L} & \frac{\partial F_1}{\partial \phi_R} & \frac{\partial F_1}{\partial f} \\ \frac{\partial F_2}{\partial \phi_L} & \frac{\partial F_2}{\partial \phi_R} & \frac{\partial F_2}{\partial f} \\ \frac{\partial F_3}{\partial \phi_L} & \frac{\partial F_3}{\partial \phi_R} & \frac{\partial F_3}{\partial f} \end{bmatrix} \tag{70}$$

Simulation results are shown in Fig. 24. In this configuration, since both left wing thrust and vehicle weight generate moment in the same direction about the $x$ axis, the right wing has smaller midstroke angle than the left wing to achieve a larger moment arm to compensate the moment generated by the $y$ direction offset of c.g.. Figure 24(c) shows how the residuals of trim equations change with iteration. Both trim equation and control parameters converge fast and at the same rate. Because the flap amplitude of the wings are same, the flap frequency converges to the same value of 18.5 Hz. This value is smaller than the experimental value of 20 Hz for the real hummingbird MAV in hovering flight. This is due to the fact that the aeroelastic model tends to predict higher lift than the experiment, as shown in Fig. 19.

## Conclusions

The paper discusses the development of a coupled aeroelastic framework for highly flexible flapping wings in hover. The aeroelastic model consists of an unsteady aerodynamic model coupled with a nonlinear structural model. This model is used to simulate an in-house developed flapping MAV wing, and predictions are compared with experimental data.

Nonlinear beam and shell elements based on geometrically exact total-Lagrangian beam and shell theories were developed for the structural analysis. This model was then validated for both static and dynamic loading conditions by comparing with a commercial FEA software. Simultaneously, an unsteady aerodynamic model was also developed. Systematic validation of the aerodynamic model was carried out by comparing with both test data and in-house CFD results on rigid flapping wings. After both models were validated independently, they were coupled to develop a high-fidelity aeroelastic framework.

In the aeroelastic analysis, direct numerical transient analysis is performed using the Newmark-$\beta$ method. Simulation results of time history of lift force was compared with lift measurements. The predicted airfoil shape at several spanwise locations was compared with the wing-deflected shape, which was measured using the DIC technique. Both the instantaneous lift and wing-deflected shape predictions correlate well with the experimental data.

A coupled trim analysis is developed for a flapping wing MAV in hovering state. With aeroelastic analysis as the wing response model and vehicle trim equations for the hover condition, the model can be used to obtain the hover trim control inputs for different flapping MAV configurations. The hovering flight case of the robotic hummingbird was simulated in the present study, and the predicted trim control inputs (especially flapping frequency) were very similar to what was measured for the real hovering platform.

## Acknowledgments

This work was jointly supported by NASA's Vertical Lift Research Center of Excellence (VLRCOE) led by the University of Maryland with Dr. Mahendra Bhagawat as Technical Monitor (Grant number: 18691-Z8533001) and National Science Foundation (Grant number: CMMI-1663247). The authors would like to thank David Coleman for his help in carrying out experimental studies.

## References

[1]Ellington, C. P., van den Berg C., Willmott, A. P., and Thomas A. L. R., "Leading-edge Vortices in Insect Flight," *Nature*, Vol. 384, 1996, pp. 626–630.

[2]Dickinson, M. H., Lehmann, F. O., and Sane, S. P., "Wing Rotation and the Aerodynamic Basis of Insect Flight," *Science*, Vol. 284, 1999, pp. 1954–1960.

[3]Vance, J. T., Faruque, I., and Humbert, J. S., "Kinematic Strategies for Mitigating Gust Perturbations in Insects," *Journal of Bioinspiration and Biomimetics*, **8**, 016004 (2013).

[4]Van Truong, T., Le, T. Q., Park, H. C., and Byun, D., "Experimental and Numerical Studies of Beetle-Inspired Flapping Wing in Hovering Flight," *Bioinspiration & Biomimetics*, **12**, 036012 (2017).

[5]Ganguli, R., Gorb, S., Lehmann, F. O. and Mukherjee, S., "An Experimental and Numerical Study of Calliphora Wing Structure, *Experimental Mechanics*, Vol. 50, (8), 2010, pp. 1183–1197.

[6]Shahzad, A., Tian, F. B., Young, J., and Lai, J. C. S., "Aerodynamic Hovering Performance of Rigid and Flexible Wing Planform Shapes," Proceedings of the 20th Australasian Fluid Mechanics Conference, Perth, Australia, December 5–8, 2016.

[7]Sun, M., and Tang, J., "Unsteady Aerodynamic Force Generation by a Model Fruit Fly Wing in Flapping Motion," *Journal of Experimental Biology*, Vol. 205, (1), 2002, pp. 55–70.

[8]Ramamurti, R., and Sandberg, W. C., "A Three-Dimensional Computational Study of the Aerodynamic Mechanisms of Insect Flight," *Journal of Experimental Biology*, Vol. 205, (10), 2002, pp.1507–1518.

[9]Karpel, M., "Design for Active Flutter Suppression and Gust Alleviation Using State-Space Aeroelastic Modeling," *Journal of Aircraft*, Vol. 19, (3), 1996, pp. 221–227.

[10]Singh, B., and Chopra, I., "Insect-Based Hover-Capable Flapping Wings for Micro Air Vehicles: Experiments and Analysis," *AIAA Journal*, Vol. 56, (9), 2008, pp. 2115–2135.

[11]Zbikowski, R., "On Aerodynamic Modelling of an Insect-Like Flapping Wing in Hover for Micro Air Vehicles," *Philosophical Transactions of the Royal Society of London A: Mathematical, Physical and Engineering Sciences*, Vol. 360, (1791), 2002, pp. 273–290.

[12]Long, L. N., and Tracy E. F, "Object-Oriented Unsteady Vortex Lattice Method for Flapping Flight," *Journal of Aircraft*, Vol. 41, (6), 2004, pp. 1275–1290.

[13]Ansari, S. A., Zbikowski, R., and Knowles, K., "Non-linear Unsteady Aerodynamic Model for Insect-Like Flapping Wings in the Hover. Part 1: Methodology and Analysis," *Proceedings of the Institution of Mechanical Engineers*, Part G: Journal of Aerospace Engineering, Vol. 220,(2), 2006, pp. 61–83.

[14]Ansari, S. A., Zbikowski, R., and Knowles, K. "Non-linear Unsteady Aerodynamic Model for Insect-like Flapping Wings in the Hover. Part 2: implementation and validation," *Proceedings of the Institution of Mechanical Engineers*, *Part G: Journal of Aerospace Engineering*, Vol. 220, (3), 2006, pp. 169–186.

[15]Birch, J. M., and Dickinson, M. H., "The Influence of Wing Wake Interactions on the Production of Aerodynamic Forces in Flapping Flight", Journal of Experimental Biology, Vol. 206, (13), July 2003.

[16]Gogulapati, A., Friedmann, P., Kheng, E., and Shyy, W., "Approximate Aeroelastic Modeling of Flapping Wings in Hover," *AIAA Journal*, Vol. 51, (3), March 2013, pp. 567–583.

[17]Coleman, D., and Benedict, M., "Design, Development and Flight-Testing of Robotic Hummingbird," Proceedings of the American Helicopter Society 71st Annual Forum, Virginia Beach, VA, May 5–7, 2015.

[18]Coleman, D., Gakhar, K., and Benedict, M., "Experimental Studies towards Understanding the Aeromechanics of a Flexible Robotic Hummingbird Wing in Hover," Proceedings of the 73rd Annual AHS International Forum and Technology Display, Fort Worth, TX, May 9–11, 2017.

[19]Pai, P. F., *Highly Flexible Structures: Modeling, Computation, and Experimentation*, AIAA, Reston, VA, 2007.

[20]Pai, P. F, Robert D. C, and Zaichun F., "High-Fidelity Total-Lagrangian Geometrically Exact Modeling and Analysis of Highly Flexible Plates/Shells,' Proceedings of the 53rd AIAA/ASME/ASCE/AHS/ASC Structures, Structural Dynamics and Materials Conference and 20th AIAA/ASME/AHS Adaptive Structures Conference 14th AIAA, 2012.

[21]Pai, P. F, Robert D. C., and Zaichun F., "Geometrically Exact Displacement-Based Shell Theory," *Thin-Walled Structures*, Vol. 70, 2013, pp. 1–18.

[22]Pai, P. F., and Schulz, M. J., "Shear Correction Factors and an Energy-Consistent Beam Theory," *International Journal of Solids and Structures*, Vol. 36, (10), 1999, pp. 1523–1540.

[23]Pai, P. F., "Three Kinematic Representations for Modeling of Highly Flexible Beams and Their Applications," *International Journal of Solids and Structures*, Vol. 48, (19), 2011, pp. 2764–2777.

[24]Halder, A., and Benedict, M., "Understanding the Effect of Blade Flexibility on Cycloidal Rotor Performance in Hover," Proceedings of the American Helicopter Society Technical Meeting, San Francisco, CA, January 20–22, 2016.

[25]Katz, J., and Plotkin, A., *Low-Speed Aerodynamics*, Cambridge University Press, Cambridge, UK, 2000.

[26]Leishman, J. G., *Helicopter Aerodynamics*, Cambridge University Press, Cambridge, UK, 2006.

[27]Yang, X., Badrya, C., Lankford, J., and Benedict, M., "CFD Analysis for Flexible Flapping Wing in Hover Flight," Proceedings of the AHS International 74th Annual Forum, Phoenix, AZ, May 14–17, 2018.